

In Vivo Quantitative MR Imaging of Bound and Pore Water in Cortical Bone¹

Mary Kate Manhard, MS
R. Adam Horch, PhD
Daniel F. Gochberg, PhD
Jeffrey S. Nyman, PhD
Mark D. Does, PhD

Purpose:

To translate and evaluate an in vivo magnetic resonance (MR) imaging protocol for quantitative mapping of collagen-bound and pore water concentrations in cortical bone that involves relaxation-selective ultrashort echo time (UTE) methods.

Materials and Methods:

All HIPAA-compliant studies were performed with institutional review board approval and written informed consent. UTE imaging sequences were implemented on a clinical 3.0-T MR imaging unit and were used for in vivo imaging of bound and pore water in cortical bone. Images of the lower leg and wrist were acquired in five volunteers each (lower leg: two men and three women aged 24, 24, 49, 30, and 26 years; wrist: two men and three women aged 31, 23, 25, 24, and 26 years) to generate bound and pore water concentration maps of the tibia and radius. Each volunteer was imaged three times, and the standard error of the measurements at the region-of-interest (ROI) level was computed as the standard deviation across studies, pooled across volunteers and ROIs.

Results:

Quantitative bound and pore water maps in the tibia and radius, acquired in 8–14 minutes, had per-voxel signal-to-noise ratios of 18 (bound water) and 14 (pore water) and inter-study standard errors of approximately 2 mol ¹H per liter of bone at the ROI level.

Conclusion:

The results of this study demonstrate the feasibility of quantitatively mapping bound and pore water in vivo in human cortical bone with practical human MR imaging constraints.

©RSNA, 2015

An earlier incorrect version of this article appeared online. This article was corrected on July 24, 2015.

¹From the Departments of Biomedical Engineering (M.K.H., M.D.D.), Radiology (R.A.H., D.F.G.), and Orthopedic Surgery and Rehabilitation (J.S.N.), Vanderbilt University, 1161 21st Ave S, AA-1105 MCN, Nashville, TN 37232-2310. Received February 19, 2014; revision requested March 26; revision received January 14, 2015; accepted January 22; final version accepted February 24. **Address correspondence** to M.D.D. (e-mail: mark.does@vanderbilt.edu).

Fracture fractures are an increasingly prevalent challenge in health care, and the number of fractures continues to increase with the rapidly growing elderly population (1). The current standard for diagnosing fracture risk comprises measurements of bone mineral density (BMD), primarily with dual-energy x-ray absorptiometry. However, bone health and fracture risk depend on many factors other than BMD, such as architecture, collagen content, and porosity. In addition, clinical risk factors such as age, previous fracture, family history, and use of corticosteroids can affect the fracture resistance of bone (2). Several methods have been developed to improve fracture risk assessment (3), such as quantitative ultrasonography of bone to reflect material information (4–6), quantitative computed tomography to measure trabecular volumetric bone density and cortical structure (7–9), and the Web-based Fracture Risk Assessment Tool, or FRAX, to account for clinical risk factors in addition to BMD measurements (10,11). In previous work, there has been substantial progress in magnetic resonance (MR) imaging methods for the evaluation of bone (12–15).

Through a variety of hydrogen 1 (^1H) MR spectroscopy studies (16,17) of ex vivo cortical bone samples, the contributions and relaxation characteristics of signals from water in pores and water bound to the collagen matrix have been characterized. MR spectroscopy signals of short T2 (approximately 400 μsec) are due to collagen-bound water, and signals of longer T2 (1 msec to 1 sec) are primarily due to pore water. In similar samples, the bound and pore water ^1H MR spectroscopy signal amplitudes have been shown to correlate with mechanical properties,

including yield stress, peak stress, and elastic toughness (18–20). Bone specimens with a greater concentration of bound water tend to have high peak and yield stress values and elastic toughness, whereas specimens with a greater concentration of pore water are generally associated with higher porosity and lower peak stress, yield stress, and toughness. However, it is necessary to distinguish between the bound and pore water signals, because their sum has little or no relationship to mechanical properties (20).

Bound and pore water signals can be discriminated on the basis of relaxation times by using wide-bandwidth T2-selective adiabatic radiofrequency (RF) pulses (21). Use of these pulses in conjunction with an ultrashort echo time (UTE) acquisition allows imaging of bound and pore water signal (22). The double adiabatic full passage (DAFP) sequence uses two consecutive adiabatic RF pulses to suppress bound water signals while retaining pore water magnetization to near its sequence equilibrium state. The adiabatic inversion recovery (AIR) sequence uses a single adiabatic RF pulse followed by an appropriate delay (inversion time) to selectively null pore water magnetization while allowing bound water magnetization to return to near its equilibrium state. In both cases, longitudinal magnetization is excited by a hard RF pulse immediately following the magnetization preparation, resulting in a signal that is primarily from pore water or bound water, respectively, for the DAFP and AIR sequences. The pulse sequence diagram for these sequences is given in Figure 1. Signal equations and a more detailed description of these methods can be found in prior works (21,22).

These sequences have previously been validated in whole human cadaveric bones with a clinical 3.0-T system

against nonlocalized measures of small bone specimens extracted from the whole bones (22). The purpose of our study was to translate and evaluate an in vivo MR imaging protocol for quantitative mapping of collagen-bound and pore water concentrations in cortical bone with relaxation-selective UTE methods.

Materials and Methods

A patent regarding the technology evaluated in this manuscript is held by R.A.H., D.F.G., J.S.N., and M.D.D.

Subjects

All studies were compliant with the Health Insurance Portability and Accountability Act, were approved by the institutional review board, and included written informed consent. Eligible volunteers included 20–80-year-old healthy adults. Exclusion criteria included volunteers with non-MR imaging compatible implants or cerebral aneurysm clips; volunteers who may have had shrapnel embedded in their bodies; volunteers younger than 20 years of age; pregnant women; and volunteers



Advance in Knowledge

- MR imaging of cortical bone water can provide quantitative measures of bound and pore water concentrations with standard errors of approximately 2 mol hydrogen 1 per liter of bone in the tibia and radius.

Implication for Patient Care

- Quantitative MR imaging maps of bound and pore water in cortical bone may potentially offer diagnostic information on bone quality within the tibia or radius.

Published online before print

10.1148/radiol.2015140336 Content codes:  

Radiology 2015; 277:221–229

Abbreviations:

AIR = adiabatic inversion recovery
 DAFP = double adiabatic full passage
 HS8 = eighth-ordered hyperbolic secant
 RF = radiofrequency
 ROI = region of interest
 SNR = signal-to-noise ratio
 UTE = ultrashort echo time

Author contributions:

Guarantors of integrity of entire study, M.K.M., J.S.N., M.D.D.; study concepts/study design or data acquisition or data analysis/interpretation, all authors; manuscript drafting or manuscript revision for important intellectual content, all authors; manuscript final version approval, all authors; literature research, M.K.M., M.D.D.; experimental studies, M.K.M., R.A.H., M.D.D.; statistical analysis, M.K.M., J.S.N., M.D.D.; and manuscript editing, all authors

Funding:

This research was supported by the National Institutes of Health (grant EB014308).

Conflicts of interest are listed at the end of this article.

Figure 1

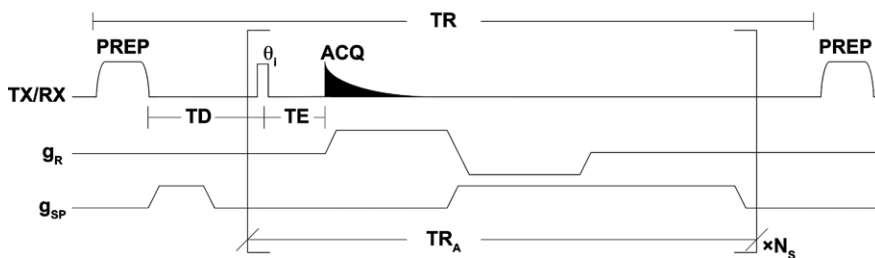


Figure 1: Diagram of the three-dimensional UTE pulse sequence. In this sequence, the preparation (*PREP*) pulse is a double eighth-ordered hyperbolic secant (HS8) pulse for DAFP and a single HS8 pulse for AIR, and *TD* is the time delay between the end of the preparation pulse and the start of data acquisition. The effective inversion recovery time $T_I = TD + TR_A \cdot N_S/2$, where N_S radial spokes are acquired with period TR_A during every repetition time (*TR*) period. *ACQ* = acquisition, g_R = readout gradient, g_{SP} = spoiler gradient, *RX* = receive RF, *TX* = transmit RF.

with a history of fragility fracture, cancer, chronic steroid use, osteogenesis imperfecta, Paget disease or other congenital bone disease, diabetes, bisphosphonate use, medical contraindication to MR imaging, or drug or alcohol abuse. The wrists in five healthy volunteers (two men and three women aged 31, 23, 25, 24, and 26 years) and the lower legs in five healthy volunteers (two men and three women aged 24, 24, 49, 30, and 26 years) were imaged three times each, with no more than 5 weeks between examinations. The subjects provided informed consent between August 2013 and August 2014.

Imaging Protocol

By using a 3.0-T Achieva MR imaging unit (Philips, Best, the Netherlands), leg studies were performed with 1.5-mm nominal isotropic resolution by using a knee eight-channel receive coil and the body coil for signal transmission. Wrist studies were performed with 1.2-mm nominal isotropic resolution by using a wrist eight-channel receive coil and the body coil for signal transmission. Wrist studies were performed with the volunteer lying in the prone position with the arm extended above the head. A short-T2 reference phantom (CuSO₄-doped 10% H₂O/90% D₂O in a 10-mm MR spectroscopy tube) in the field of view was used to convert signal intensity into absolute units of concentration (moles of ¹H per liter of bone). Another pair of reference phantoms with longer

T2s were used in measuring the relative receive field in the first phantom, as described below.

Bound and pore water maps were generated by using the AIR and DAFP sequences, respectively, and a conventional UTE sequence was performed for anatomic reference. All examinations, including positioning for both the tibia and the radius, took approximately 1 hour. The following parameters were used for the AIR sequence: repetition time, 400 msec; inversion time, 85 msec; and adiabatic inversion with a 10-msec, 3.5-kHz HS8 pulse. The DAFP sequence was performed with the following parameters: repetition time, 615 msec (for the wrist) or 400 msec (for the leg); time delay, 5 msec; and two consecutive HS8 pulses. Signal acquisition for the DAFP and AIR sequences was accomplished by acquiring 124 samples (for the wrist) or 171 samples (for the leg) along each of 20000 (for the wrist) or 33792 (for the leg) radial half-spokes in k-space. Studies were accelerated by acquiring $N_S = 16$ spokes per magnetization preparation (Fig 1), with a 3.18-msec repetition time per spoke, resulting in imaging times of approximately 8–12 minutes for the AIR and DAFP sequences in the wrist and 14 minutes for each study in the leg. Magnetization was excited with a 115- μ sec hard RF pulse and a variable flip angle schedule (initial prescribed flip angle, $\theta_1 = 12.5^\circ$; effective total flip angle, $\theta_E = 60^\circ$) to

generate approximately constant transverse magnetization for all 16 spokes (23). The effective echo time, as measured from the center of the RF excitation pulse to the start of acquisition, was 127.5 μ sec. The conventional UTE image in each study was obtained with a repetition time of 2.5 msec, an echo time of 62.5 μ sec, and a 25- μ sec, 6° flip excitation pulse. The maximum gradient amplitudes and slew rates of the system were used in all studies. The repetition times were dictated by U.S. Food and Drug Administration–defined RF power deposition limits.

The receive-coil sensitivity map was characterized by computing the ratio of two low-resolution T1-weighted images (repetition time, 447 msec; echo time, 26 msec; voxel size, $2 \times 2 \times 6$ mm) by using the knee coil for receiving for the first image and the body coil for receiving for the second. Because the signal in the cortical bone region was very low on these T1-weighted images, the sensitivity map was smoothed by using map values from surrounding voxels within an apodized 11×11 window. The signal in the short-T2 reference phantom was also low in the sensitivity maps, so the sensitivity for this phantom was estimated from the mean relative sensitivity of two longer-T2 reference phantoms placed on either side of the short-T2 phantom.

Image Analysis

Images were reconstructed by using standard Philips base code or, for data acquired after a system hardware repair and gradient recalibration, were reconstructed offline by using measured gradient trajectories (24) and standard density compensation and gridding methods (25). Bound and pore water concentrations were computed on a voxel-by-voxel basis by using previously published signal equations (22) and were converted to absolute units of water equivalent concentration by using the reference marker signal, which had a known concentration of 11.11 mol ¹H per liter of bone. The blurring-induced signal loss that results from having signal with a T2* approximately equal to the radial acquisition time

Figure 2

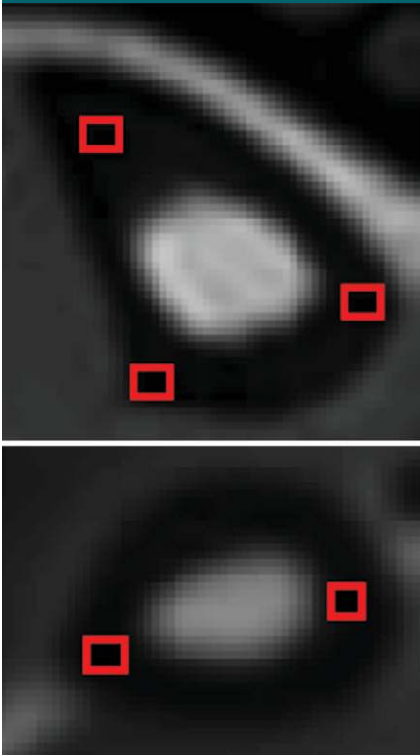


Figure 2: Example ROI locations (red boxes) in the tibia (top) and wrist (bottom). ROIs were 3–6 voxels within an axial section, through three sections.

was empirically estimated by simulating the effect of blurring by using bone geometry (22). In the signal equations, for bound and pore water, respectively, T_1 was defined as 290 and 450 msec (22), and T_2^* was defined as 350 and 2600 μ sec (26).

Statistical Analysis

For ease of manually defining regions of interest (ROIs), images were upsampled by a factor of two by using bicubic interpolation, and ROIs were chosen by a single observer (M.K.M., with 3 years of experience) with reference to anatomic landmarks. The size of each ROI was 12 or 6 voxels per section for the tibia and radius, respectively, through a 4.5-mm section thickness. In both the tibia and the radius, the ROIs were chosen close to the midpoint of the diaphysis. Keeping the distance from the distal end of the radius or tibia to the center of the field of view constant between

Figure 3

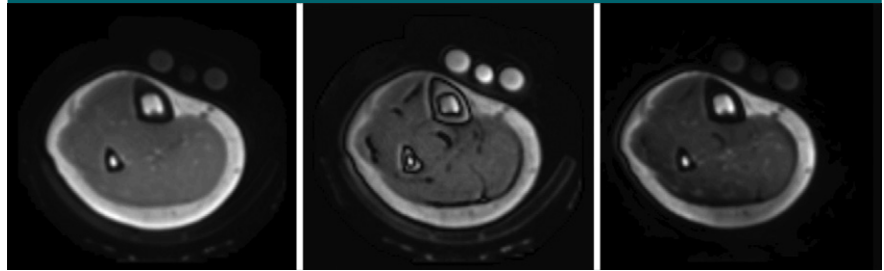


Figure 3: Representative axial MR imaging sections obtained in the lower leg of one volunteer by using the three UTE protocols: conventional UTE (left), AIR (middle), and DAFP (right).

repeated studies ensured consistency in location. Examples of ROI locations are shown in Figure 2. There were three ROIs in the tibia, corresponding to the anterior, medial, and posterior parts of the cortical bone. Two ROIs were defined in the medial and lateral parts of the radius. Voxels near the edge of the bone were avoided to minimize partial-volume effects.

The standard deviation of image noise per voxel was measured as the $\text{mean}/\sqrt{\pi}/2$ from a background region prior to upsampling of the image, and the standard deviations of the bound and pore water concentrations were then computed from this value through propagation of error. The per-voxel signal-to-noise ratio (SNR) was defined as the bound or pore water concentration within the cortical bone divided by the computed standard deviation of the bound or pore water concentration. Inter-study variability was evaluated for each volunteer and ROI as the standard deviation of the ROI means across three repeated studies. With the assumption that inter-study variability was independent of volunteer and ROI, the pooled standard deviation was also computed for each of the four protocols (DAFP and AIR of the tibia and radius).

Results

To demonstrate general image quality, Figure 3 shows representative raw magnitude image sections of the leg in one volunteer obtained by using all three UTE protocols—conventional UTE, AIR, and DAFP; images of the wrist

looked similar. The bone tissue signal intensity on the conventional UTE and DAFP images looks dark compared with that of the surrounding tissue because of the difference in proton density between bone and fat or muscle, but the signal in the bone was greater than the noise in all cases.

Quantitative bound and pore water maps in all five volunteers are presented in Figures 4 and 5. Figure 4 shows representative sections of bound and pore water maps in the tibia overlaid on conventional UTE images. Figure 5 shows similar images of the wrist, with bound and pore water maps overlaid on images of the radius. Across subjects and repeated studies, the mean per-voxel standard deviation of the bound and pore water maps was 1.39 and 0.74 mol ^1H per liter of bone, respectively, and was approximately equal for the tibia and radius studies. Correspondingly, the per-voxel SNR was 18 for bound water maps and 14 for pore water maps.

The repeatability of the parameter maps can be qualitatively assessed in Figure 6, which shows maps from the three repeated studies in one subject in the tibia and in one subject in the wrist. Results of quantitative evaluation of mean bound and pore water concentrations among the three imaging sessions per subject with inter-study variability of signals are shown in Tables 1 and 2 and are summarized in Figure 7. In the tibia and the radius, bound water concentrations were approximately 28 and 35 mol ^1H per liter of bone, respectively, and corresponding pore water concentrations were

Figure 4

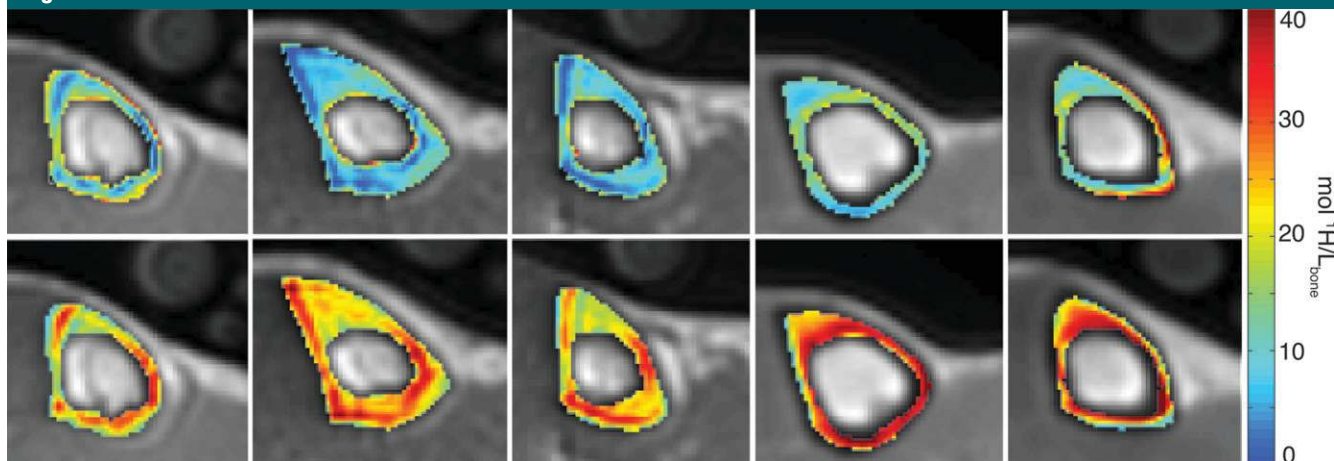


Figure 4: Axial MR images obtained in the lower leg in all five subjects; images are conventional UTE images overlaid with pore (top row) and bound (bottom row) water maps in the tibia.

Figure 5

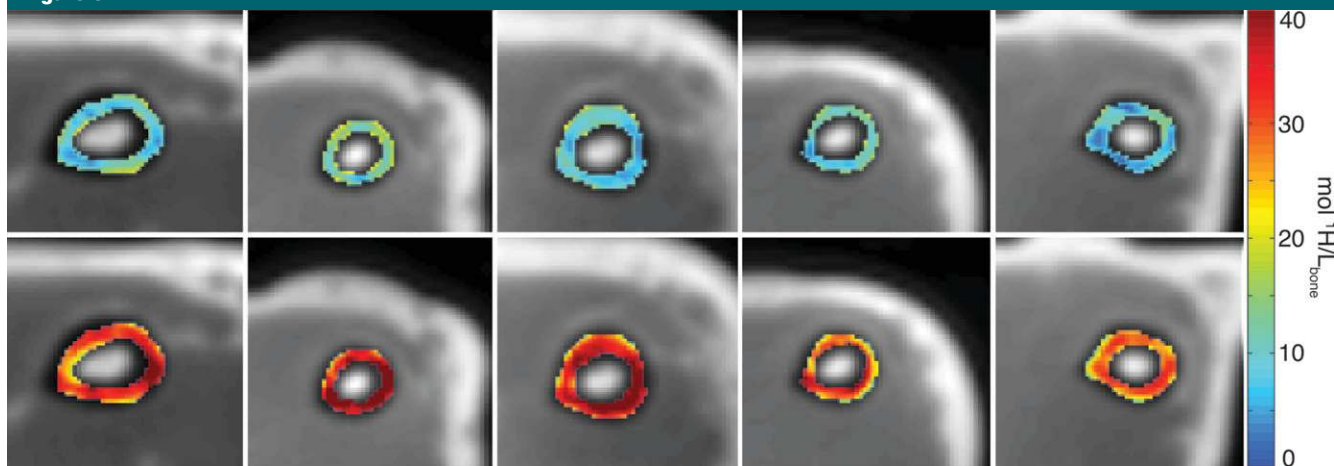


Figure 5: Axial MR images obtained in the wrist in all five subjects; images are conventional UTE images overlaid with pore (top row) and bound (bottom row) water maps in the radius.

approximately 7 and 6 mol ^1H per liter of bone. These values were similar to those in previous ex vivo observations in the femur (22). Bound and pore water are generally inversely correlated, especially in the larger anterior section of the tibia. As expected, the healthy volunteers in this study had relatively high bound water and low pore water concentrations. Tabulated for each ROI, the inter-study standard deviation in ROI means (Tables 1 and 2 and error bars in Fig 7) were generally similar in magnitude, with a mean of 1.93 mol ^1H per liter of bone

(range, 0.07–4.1 mol ^1H per liter of bone). Given the ROI sizes, these inter-study variations were generally greater than expected from intrinsic noise levels alone (see above), indicating some systematic variation from study to study, the causes of which are discussed below.

Discussion

The DAFP and AIR methods of measuring pore and bound water concentrations, respectively, in cortical bone were demonstrated in vivo in the radius

and tibia. The radius and the tibia are excellent sites for MR imaging because of their size and accessibility for coils; additionally, imaging measurements in these bones have been shown to be associated with fracture risk (3). These methods have no ionizing radiation and allow for new quantitative measurements that are known to reflect the material properties of bone (18–20). In particular, bound water is not detectable with conventional bone imaging methods but is indirectly a marker of collagen matrix integrity and has shown correlations with the toughness

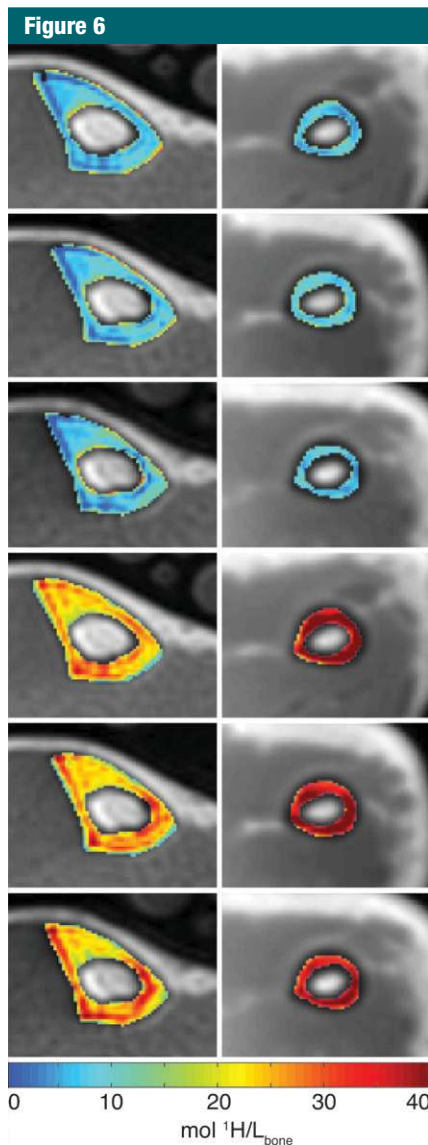


Figure 6: Representative axial MR images of the tibia in one subject (left column) and the radius in another (right column); images are conventional UTE images with pore (top) and bound (bottom) water maps overlaid for three repeated studies.

of bone (19,20). Low bound water measurements could account for the disproportionate increase in fracture risk compared with the decrease in bone density measurements in type 2 diabetes or in aging populations that have demonstrated increased brittleness that cannot be measured with current x-ray methods (27,28). Pore water is an indirect measure of porosity;

Table 1			
Inter-Study Means and Standard Deviations in the Tibia			
Subject and ROI	Bound Water	Pore Water	
Subject 1			
ROI 1	28.61 ± 1.37	2.86 ± 0.41	
ROI 2	23.28 ± 0.36	8.59 ± 1.53	
ROI 3	25.70 ± 0.58	11.30 ± 2.17	
Subject 2			
ROI 1	23.11 ± 0.75	5.53 ± 0.07	
ROI 2	29.93 ± 1.54	3.47 ± 0.34	
ROI 3	26.45 ± 1.98	8.99 ± 0.76	
Subject 3			
ROI 1	18.57 ± 1.96	9.24 ± 0.83	
ROI 2	32.14 ± 1.61	1.85 ± 0.59	
ROI 3	25.10 ± 1.92	7.43 ± 0.78	
Subject 4			
ROI 1	24.05 ± 0.53	8.56 ± 1.29	
ROI 2	31.67 ± 1.43	6.53 ± 1.00	
ROI 3	32.57 ± 1.74	10.34 ± 2.23	
Subject 5			
ROI 1	27.74 ± 3.14	8.10 ± 0.79	
ROI 2	31.93 ± 4.14	8.74 ± 0.70	
ROI 3	36.98 ± 2.92	8.23 ± 1.22	
Mean	27.86 ± 2.00*	7.32 ± 1.15*	

Note.—Data are mean water concentrations (in moles of ¹H per liter of bone) ± standard deviations.
*Pooled standard deviation across all subjects and ROIs.

as pore water increases, porosity increases (29). Therefore, we postulate that subjects at high risk for fragility fractures will generally have high pore water and/or low bound water, although more studies need to be performed to justify this claim. In future studies, these methods will be applied to subjects with poor bone health, such as postmenopausal women, to evaluate changes in bound and pore water in response to treatment.

In contrast to previous MR imaging studies of human bone in vivo, which provided structural information (12,30) or information regarding net cortical bone water (31–33), our methods specifically discriminated between signals from bound water and those from pore water. (Although one of these previous studies [32] included soft-tissue signal suppression, which likely suppressed some portion of the pore water signal.)

Table 2			
Inter-Study Means and Standard Deviations in the Radius			
Subject and ROI	Bound Water	Pore Water	
Subject 1			
ROI 1	28.65 ± 0.49	4.23 ± 1.12	
ROI 2	28.99 ± 2.51	6.37 ± 0.45	
Subject 2			
ROI 1	42.97 ± 1.91	6.33 ± 2.67	
ROI 2	34.13 ± 0.69	6.72 ± 3.55	
Subject 3			
ROI 1	37.53 ± 1.28	6.20 ± 1.93	
ROI 2	40.87 ± 3.01	5.09 ± 1.38	
Subject 4			
ROI 1	33.93 ± 3.56	4.52 ± 0.44	
ROI 2	35.38 ± 3.80	12.87 ± 2.52	
Subject 5			
ROI 1	32.33 ± 3.37	5.01 ± 1.83	
ROI 2	33.79 ± 2.72	4.07 ± 1.41	
Mean	34.86 ± 2.59*	6.14 ± 1.97*	

Note.—Data are mean water concentrations (in moles of ¹H per liter of bone) ± standard deviations.
*Pooled standard deviation across all subjects and ROIs.

An alternate approach for distinguishing between bound and pore water signals in cortical bone by using only T2* differences and bicomponent analysis of the signal decay with echo time has been demonstrated ex vivo (26). If incorporated into fast two-dimensional UTE acquisitions across a wide range of echo times (31), this approach may offer another clinically viable MR imaging protocol for bound and pore water measurement in vivo.

Our methods directly measure bound and pore water content, so they do not require multiple echo times or as high of an SNR as bicomponent analysis needs in order to measure bound and pore water signal by using T2* differences. Bicomponent analysis can be further confounded when the underlying signal has more than two T2* components or in the presence of fat signal, which does not decay exponentially owing to chemical shift differences with water. In addition, similar to protocols in some previous quantitative MR imaging studies of cortical bone (26,27), the DAFP and AIR protocols presented

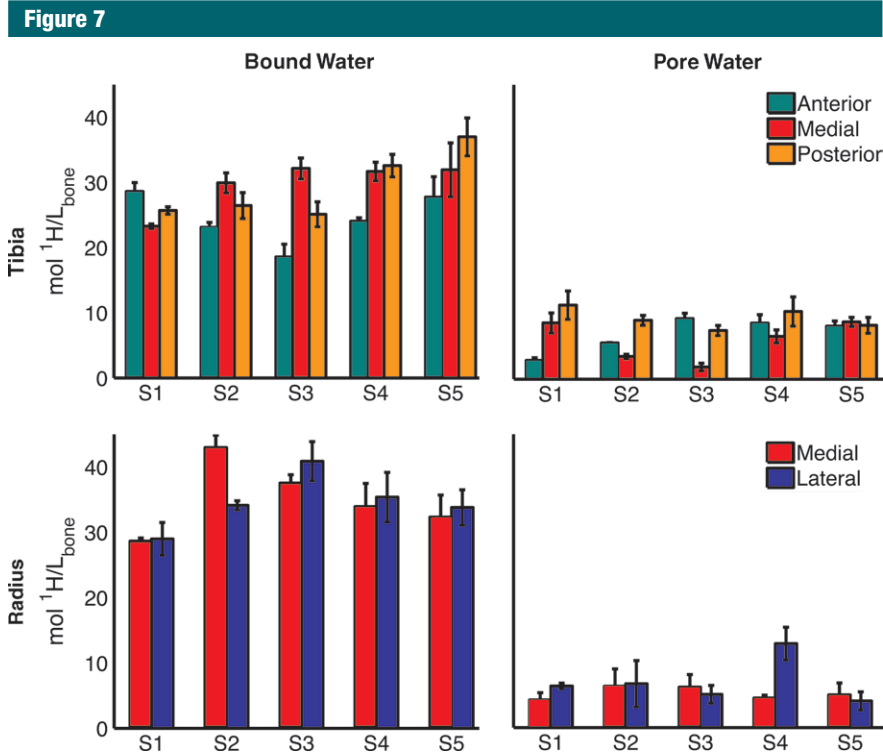


Figure 7: Bar graphs show quantified signal in the five ROIs in the tibia and radius in all five subjects (S1, S2, S3, S4, S5). Bars = mean in the ROIs over the three repeated studies, error bars = inter-study variability (standard deviation between the three studies).

here involved the use of reference phantoms to convert signals into absolute units of proton concentration. This is especially important when separating two distinct signals from the bone, because a change in the relative fractions of these two signals could be due to a specific change in either or both.

As for many quantitative MR imaging protocols, the primary limitations of the methods presented here were precision and imaging time. The per-voxel intra-study variability alone was approximately 0.8 mol ¹H per liter of bone in imaging times of 8–14 minutes, but the pooled standard deviation of signal intensities across repeated studies was roughly twice that (Tables 1 and 2), indicating room for improvement in precision that was independent of raw SNR.

The effect of excitation flip angle calibration on our measurements was independently investigated by acquiring B_1^+ maps (34) repeatedly in one subject five times in the tibia and three

times in the radius, with repositioning between measurements. By using measured B_1^+ values in the bone and reference markers from these studies, the prescribed B_1^+ , and the mean bound and pore water concentrations listed in Tables 1 and 2, the effects of B_1^+ variation between studies on bound and pore water concentrations were calculated. These calculations showed that B_1^+ variations resulted in standard deviations in bound and pore water concentrations, respectively, of 0.80 and 0.30 mol ¹H/L_{bone} in the tibia and slightly lower values in the radius. In principle, this source of signal variation can be accounted for with B_1^+ mapping and/or better RF calibration protocols.

The remaining systematic inter-study signal variation was likely due to variations in ROI placement and associated partial-volume effects. As a simple test, signal intensities were recomputed for whole-section ROIs, and the inter-study pooled standard deviation decreased by an average of 0.5 mol ¹H per

liter of bone. Thus, defining larger ROIs would tend to reduce the inter-study variance, although at the expense of losing sensitivity to more localized changes in bound or pore water concentrations. Some more sophisticated signal analysis that considers the distribution of bound and pore water throughout the entire bone volume might offer both low inter-study variance and high sensitivity to local or global changes in bone characteristics. Also, higher resolution studies may permit more reproducible, automated ROI placement and will minimize partial-volume averaging effects. Spatial resolution may be a particularly important limitation when imaging patients with osteoporosis, who tend to have thin bone cortex.

Higher resolution images will require both faster imaging protocols and some increase in SNR. The use of dedicated or specialized RF coils for signal reception offers the best opportunity to improve resolution and imaging time, albeit with a smaller field of view. Beyond hardware improvements, reduced (35) or anisotropic (36,37) field of view methods might be effective in increasing resolution or in enabling access to regions such as the femoral neck that would otherwise require a relatively large three-dimensional field of view and long imaging time. Similarly, another possible approach is to use two-dimensional rather than three-dimensional UTE acquisitions. Current two-dimensional UTE protocols use half-pulse RF excitation to keep echo times short (38–40), but signal amplitudes from these methods are very sensitive to gradient waveform calibration, making their use for quantitative methods a challenge. A two-dimensional UTE protocol that is relatively insensitive to gradient performance has been proposed (41), but it comes with an additional SNR cost. Finally, given the relatively sparse nature of the bound and pore water maps, model-based reconstruction or compressed sensing may offer avenues to reducing imaging time.

Despite the current limitations of the DAFP and AIR methods, our results (Tables 1 and 2, and Fig 7) demonstrate potential for these methods to

provide clinical insight into changes in bone health. Using the pooled standard deviation estimates as the standard error (SE) for each method and bone, the smallest significant statistical difference detectable between repeated studies in a given individual was $t_{\alpha, \nu} \cdot \sqrt{2} \cdot \text{SE}$, where $t_{\alpha, \nu}$ is the t statistic for a significance level of α and a two-tailed test and ν is the number of degrees of freedom (27). At an α of .05 and $\nu = (n - k)$, with $n =$ (number of subjects times number of ROIs times number of studies) (45 for the tibia and 30 for the radius) and $k =$ (number of subjects times number of ROIs) (15 for the tibia and 10 for the radius), on the basis of data from this study, these smallest statistical differences were 3.3 and 5.8 mol ^1H per liter of bone in the pore water and 5.7 and 7.5 mol ^1H per liter of bone in the bound water of the tibia and radius, respectively. Given the estimates for reducing inter-study variability through quantitative B_1^+ mapping and whole-bone data analysis provided above, these smallest statistical differences may decrease to 2.4 and 3.4 mol ^1H per liter of bone in the pore water and 4.4 and 6.8 mol ^1H per liter of bone in the bound water of the tibia and radius, respectively. Given the limit that the only factor in inter-study repeatability is thermal noise, with the current SNR, these differences would decrease further to 1.9 and 2.5 mol ^1H per liter of bone in the pore water and 3.8 and 4.7 mol ^1H per liter of bone in the bound water of the tibia and radius, respectively.

Although these values are not small compared with the variation in bound and pore water measures across subjects here, only healthy and relatively young volunteers were included in our study, which gave a relatively small range of bound and pore water values. A greater range of values would be expected between healthy and unhealthy bones. In previous *ex vivo* studies of cortical bone samples(20,22), bound water measurements in the femur ranged from approximately 11 to 24 mol ^1H per liter of bone, while pore water measurements ranged from approximately 5 to 30 mol ^1H per liter of

bone. These bone samples came from 43 cadavers with unknown bone health (age range at death, 21–105 years), so this wider range (13 and 25 mol ^1H per liter of bone for bound and pore water) may reflect a more clinically relevant range of values than that seen in the healthy subjects in our study. Further studies are needed to determine the diagnostic potential of these measurements for specific clinical conditions.

In conclusion, the results of our study demonstrate that quantitative MR imaging that is selective for bound or pore water in cortical bone can be practically performed in vivo, yielding bound and pore water maps with standard errors of approximately 2 mol ^1H per liter of bone.

Disclosures of Conflicts of Interest: **M.K.M.** disclosed no relevant relationships. **R.A.H.** Activities related to the present article: holds a patent (U.S. patent 8,923,948) related to the technology reported in this article. Activities not related to the present article: none to disclose. Other relationships: none to disclose. **D.F.G.** Activities related to the present article: holds a patent (U.S. patent 8,923,948) related to the technology reported in this article. Activities not related to the present article: none to disclose. Other relationships: none to disclose. **J.S.N.** Activities related to the present article: holds a patent (U.S. patent 8,923,948) related to the technology reported in this article. Activities not related to the present article: none to disclose. Other relationships: none to disclose. **M.D.D.** Activities related to the present article: holds a patent (U.S. patent 8,923,948) related to the technology reported in this article. Activities not related to the present article: none to disclose. Other relationships: none to disclose.

References

1. NIH Consensus Development Panel on Osteoporosis Prevention, Diagnosis, and Therapy. Osteoporosis prevention, diagnosis, and therapy. *JAMA* 2001;285(6):785–795.
2. Kanis JA. Diagnosis of osteoporosis and assessment of fracture risk. *Lancet* 2002;359(9321):1929–1936.
3. Link TM. Osteoporosis imaging: state of the art and advanced imaging. *Radiology* 2012; 263(1):3–17.
4. Glüer CC, Eastell R, Reid DM, et al. Association of five quantitative ultrasound devices and bone densitometry with osteoporotic vertebral fractures in a population-based sample: the OPUS Study. *J Bone Miner Res* 2004; 19(5):782–793.
5. Krieg MA, Barkmann R, Gonnelli S, et al. Quantitative ultrasound in the management of osteoporosis: the 2007 ISCD Official Positions. *J Clin Densitom* 2008;11(1):163–187.
6. Guglielmi G, Adams J, Link TM. Quantitative ultrasound in the assessment of skeletal status. *Eur Radiol* 2009;19(8):1837–1848.
7. Burrows M, Liu D, McKay H. High-resolution peripheral QCT imaging of bone microstructure in adolescents. *Osteoporos Int* 2010;21(3):515–520.
8. Liu XS, Zhang XH, Sekhon KK, et al. High-resolution peripheral quantitative computed tomography can assess microstructural and mechanical properties of human distal tibial bone. *J Bone Miner Res* 2010;25(4):746–756.
9. Burghardt AJ, Issever AS, Schwartz AV, et al. High-resolution peripheral quantitative computed tomographic imaging of cortical and trabecular bone microarchitecture in patients with type 2 diabetes mellitus. *J Clin Endocrinol Metab* 2010;95(11):5045–5055.
10. Kanis JA, McCloskey EV, Johansson H, Oden A, Ström O, Borgström F. Development and use of FRAX in osteoporosis. *Osteoporos Int* 2010;21(Suppl 2):S407–S413.
11. Kanis JA, Hans D, Cooper C, et al. Interpretation and use of FRAX in clinical practice. *Osteoporos Int* 2011;22(9):2395–2411.
12. Majumdar S, Genant HK, Grampp S, et al. Correlation of trabecular bone structure with age, bone mineral density, and osteoporotic status: in vivo studies in the distal radius using high resolution magnetic resonance imaging. *J Bone Miner Res* 1997;12(1):111–118.
13. Wehrli FW, Hwang SN, Ma J, Song HK, Ford JC, Haddad JG. Cancellous bone volume and structure in the forearm: noninvasive assessment with MR microimaging and image processing. *Radiology* 1998;206(2):347–357.
14. Manske SL, Liu-Ambrose T, de Bakker PM, et al. Femoral neck cortical geometry measured with magnetic resonance imaging is associated with proximal femur strength. *Osteoporos Int* 2006;17(10):1539–1545.
15. Bae WC, Chen PC, Chung CB, Masuda K, D'Lima D, Du J. Quantitative ultrashort echo time (UTE) MRI of human cortical bone: correlation with porosity and biomechanical properties. *J Bone Miner Res* 2012; 27(4):848–857.
16. Horch RA, Nyman JS, Gochberg DF, Dortch RD, Does MD. Characterization of ^1H NMR signal in human cortical bone for magnetic resonance imaging. *Magn Reson Med* 2010; 64(3):680–687.

17. Ong HH, Wright AC, Wehrli FW. Deuterium nuclear magnetic resonance unambiguously quantifies pore and collagen-bound water in cortical bone. *J Bone Miner Res* 2012;27(12):2573–2581.
18. Fernández-Seara MA, Wehrli SL, Takahashi M, Wehrli FW. Water content measured by proton-deuteron exchange NMR predicts bone mineral density and mechanical properties. *J Bone Miner Res* 2004;19(2):289–296.
19. Nyman JS, Ni Q, Nicoletta DP, Wang X. Measurements of mobile and bound water by nuclear magnetic resonance correlate with mechanical properties of bone. *Bone* 2008;42(1):193–199.
20. Horch RA, Gochberg DF, Nyman JS, Does MD. Non-invasive predictors of human cortical bone mechanical properties: T(2)-discriminated H NMR compared with high resolution X-ray. *PLoS ONE* 2011;6(1):e16359.
21. Horch RA, Gochberg DF, Nyman JS, Does MD. Clinically compatible MRI strategies for discriminating bound and pore water in cortical bone. *Magn Reson Med* 2012;68(6):1774–1784.
22. Manhard MK, Horch RA, Harkins KD, Gochberg DF, Nyman JS, Does MD. Validation of quantitative bound- and pore-water imaging in cortical bone. *Magn Reson Med* 2014;71(6):2166–2171.
23. Haacke EM, Brown RW, Thompson MR, Venkatesan R. *Magnetic resonance imaging: physical principles and sequence design*. New York, NY: Wiley, 1999; 463–465.
24. Gurney P, Pauly J, Nishimura DG. A simple method for measuring B0 eddy currents [abstr]. In: Proceedings of the Thirteenth Meeting of the International Society for Magnetic Resonance in Medicine. Berkeley, Calif: International Society for Magnetic Resonance in Medicine, 2005; 866.
25. Zwart NR, Johnson KO, Pipe JG. Efficient sample density estimation by combining gridding and an optimized kernel. *Magn Reson Med* 2012;67(3):701–710.
26. Du J, Hermida JC, Diaz E, et al. Assessment of cortical bone with clinical and ultrashort echo time sequences. *Magn Reson Med* 2013;70(3):697–704.
27. Kanis JA, Johnell O, Oden A, Dawson A, De Laet C, Jonsson B. Ten year probabilities of osteoporotic fractures according to BMD and diagnostic thresholds. *Osteoporos Int* 2001;12(12):989–995.
28. Vestergaard P. Discrepancies in bone mineral density and fracture risk in patients with type 1 and type 2 diabetes: a meta-analysis. *Osteoporos Int* 2007;18(4):427–444.
29. Biswas R, Bae W, Diaz E, et al. Ultrashort echo time (UTE) imaging with bi-component analysis: bound and free water evaluation of bovine cortical bone subject to sequential drying. *Bone* 2012;50(3):749–755.
30. Baum T, Kutscher M, Müller D, et al. Cortical and trabecular bone structure analysis at the distal radius: prediction of biomechanical strength by DXA and MRI. *J Bone Miner Metab* 2013;31(2):212–221.
31. Du J, Hamilton G, Takahashi A, Bydder M, Chung CB. Ultrashort echo time spectroscopic imaging (UTESI) of cortical bone. *Magn Reson Med* 2007;58(5):1001–1009.
32. Techawiboonwong A, Song HK, Leonard MB, Wehrli FW. Cortical bone water: in vivo quantification with ultrashort echo-time MR imaging. *Radiology* 2008;248(3):824–833.
33. Rad HS, Lam SCB, Magland JF, et al. Quantifying cortical bone water in vivo by three-dimensional ultra-short echo-time MRI. *NMR Biomed* 2011;24(7):855–864.
34. Sacolick LI, Wiesinger F, Hancu I, Vogel MW. B1 mapping by Bloch-Siegert shift. *Magn Reson Med* 2010;63(5):1315–1322.
35. Techawiboonwong A, Song HK, Wehrli FW. In vivo MRI of submillisecond T(2) species with two-dimensional and three-dimensional radial sequences and applications to the measurement of cortical bone water. *NMR Biomed* 2008;21(1):59–70.
36. Larson PZ, Gurney PT, Nishimura DG. Anisotropic field-of-views in radial imaging. *IEEE Trans Med Imaging* 2008;27(1):47–57.
37. Li C, Siefert A, Magland J, Wehrli F. Zero Echo Time (ZTE) imaging with anisotropic field-of-view [abstr]. In: Proceedings of the Twenty-First Meeting of the International Society for Magnetic Resonance in Medicine. Berkeley, Calif: International Society for Magnetic Resonance in Medicine, 2013; 762.
38. Robson MD, Gatehouse PD, Bydder M, Bydder GM. Magnetic resonance: an introduction to ultrashort TE (UTE) imaging. *J Comput Assist Tomogr* 2003;27(6):825–846.
39. Wang K, Du J, O'Halloran R, et al. Ultrashort TE spectroscopic imaging (UTESI) using complex highly-constrained backprojection with local reconstruction (HYPR LR). *Magn Reson Med* 2009;62(1):127–134.
40. Du J, Diaz E, Carl M, Bae W, Chung CB, Bydder GM. Ultrashort echo time imaging with bicomponent analysis. *Magn Reson Med* 2012;67(3):645–649.
41. Harkins KD, Does MD, Grissom WA. Iterative method for predistortion of MRI gradient waveforms. *IEEE Trans Med Imaging* 2014;33(8):1641–1647.